

Coil Geometry Learning for Short-Range Magnetic Actuation

Yuta Takahashi^{1,2}, Hayate Tajima³, Shin-ichiro Sakai⁴

Abstract—Fuel-free docking is a key operational technology for in-space assembly, resupplying space stations, sample return missions, and formation keeping of large-scale satellite swarms. The use of conventional propulsion systems, including thrusters, can cause adverse effects at short distances, such as sensor contamination, which may lead to the failure of the satellite or onboard equipment. The magnetic field interaction control generated by magnetorquers can overcome these weaknesses of propulsion. This actuation enables simultaneous control of attitude and formation control among desired satellite groups. The previous study typically uses the traditional dipole approximation model of the exact magnetic field to reduce computation cost. However, proximity operations often involve relatively short distances between satellites, which can easily compromise the effectiveness of this approximation. To avoid model errors that could result in satellite collisions, we utilize a magnetic field model described by Biot-Savart’s law, without distance approximations (Near-field model), in consideration of short-distance operations. To overcome the high computational cost associated with the coil geometry and relative states information, a learning-based magnetic field approximation is derived, and its effectiveness is shown in the docking simulation of target and chaser satellites equipped with electromagnetic coils on three axes. Our method significantly reduces the computational cost of the exact magnetic model and possesses scalability that can accommodate an increasing number of target satellites through parallel processing.

Index Terms—Distributed Space System, Multi-Agent Control, Non-Convex Programming.

I. INTRODUCTION

FUEL-free satellite docking using magnetic actuation has the potential to enhance system scalability, mission flexibility, and maximize system performance. Several studies consider the proximity operations between two satellites, including docking for space structural assembly [1]–[3], satellite separation [4], debris removal or refueling [5], and sample return missions [6]. These short-range control technologies also can be applied to a new class of science missions enabled by large ensembles small satellites [7], [8] such as satellite swarm-based antenna arrays for direct communication with small terminals on the ground [9]–[12] and on-orbit construction of space structures [13]. Thrusters have been commonly used for relative distance and absolute attitude control under the unstable dynamics; however, employing these for short-distance operations imposes a fuel limitation, reducing mission flexibility and duration. Moreover, thruster docking can result

Offline: Coil geometry calculation for coils of radius $R_{[1]}$

1) $R_{[1]}$ coils 2) Coordinate transformation 3) Circular integration

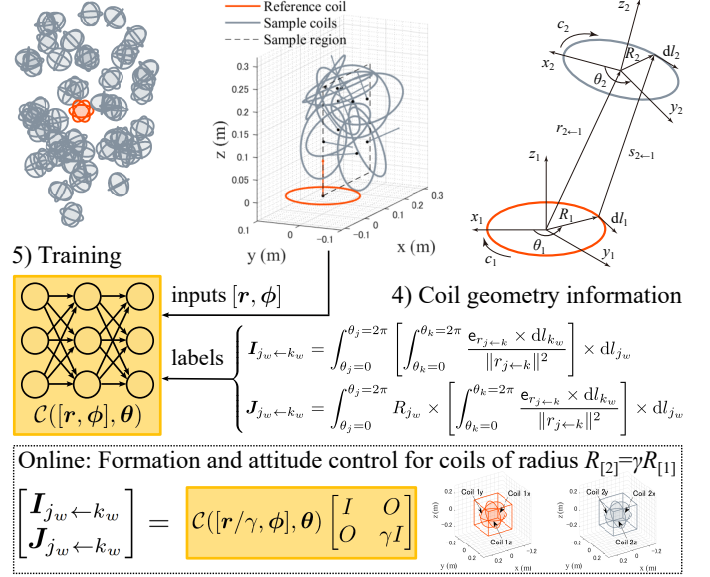


Fig. 1: Coil geometry learning presented in subsection IV.

in sensor contamination, disturbance generation, and excessive heating due to plume impact [14]–[18]. These thruster issues can lead to failures in the satellite and onboard equipment [13], [18].

Numerous studies utilize magnetorquers (MTQs) for maintaining the control of multiple satellites in relatively proximity to each other, ensuring their attitude and formation. MTQ is a conventional attitude actuator using 3-axis magnetic torques [19] and is also applied to a non-contact micro-vibration disturbance suppression [20]. Previous studies extend this to control relative positions of multiple satellites referred to as electromagnetic formation flight (EMFF) [1], [20]–[28], [28], [29]. Demonstrations of EMFF for two satellites have been conducted on the space station [29], and recent research proceeds into the large number of satellite control using magnetic field interactions [21], [23]. Some studies have proposed the simultaneous control of electromagnetic force and torque to reduce the number of attitude control devices and further conserve satellite resources [29]. This is achieved through time-integrated control, such as alternating current, which also helps mitigate the influence of the Earth’s magnetic field. Then, magnetic field interaction control enables the six-degree-of-freedom control of multiple satellites without fuel usage.

However, predicting the exact magnetic field interaction incurs a high computational burden, especially for short-range operations. The exact magnetic field model for formation flight is formulated in [26], [28], [30]. This model

¹Graduate Student, Department of Mechanical Engineering, Tokyo Institute of Technology, Ookayama Meguro, Tokyo 152-8552, Japantakahashi.y.ci@m.titech.ac.jp

²Researcher, Satellite Research and Development, Interstellar Technologies Inc., 149-7 Hiroo, Hokkaido 089-2113, Japan

³Graduate Student, Department of Advanced Energy, The University of Tokyo, 5-1-5 Kashiwanoha, Kashiwa, Chiba 277-8561, Japan

⁴Professor, Department of Spacecraft Engineering, Japan Aerospace Exploration Agency, 3-1-1 Yoshinodai, Sagami-hara, Kanagawa 252-5210, Japan

includes the circular integration-related coil geometry, and the real-time calculation is always a trade-off between accuracy and computational time. Previous research primarily employs the approximation of magnetic field models based on the assumption that the distance between coils is significantly larger than the coil radius (far-field model). While the far-field model reduces computational cost, it becomes less accurate as the distance between the coils decreases. Consequently, the desired control force cannot be achieved at short distances, resulting in inaccuracy, instability, and, in the worst case, satellite collision [31].

To this end, this study proposes a coil geometry learning associated with the exact magnetic field for real-time derivation of exact magnetic field coefficients. We integrate the proposed learning-based approximate magnetic field model into a decentralized current allocation strategy, enabling relative force and torque control without inter-agent communication. The effectiveness of this approach is demonstrated through numerical docking simulations. The overall structure of our study is as follows: Section II formulates the dynamics of an Earth-orbiting satellite and the exact magnetic model, known as the near-field model. Section III derives a communication-free decentralized current calculation for the near-field model. Unlike the previous study [32], our model incorporates the coil offset relative to the coil center. The learning-based coil geometry estimation is derived in the following section IV. Finally, section V validates the proposed learning-based current calculation by numerical simulations of satellite docking. We integrate the derived current calculation method with the Earth-orbiting satellite dynamics for electromagnetic force docking control. This section compares the docking result using a conventional far-field approximation and an exact magnetic field model. This demonstrates the proposed decentralized current calculation and accurate control of the magnetic field. The simulation results generate the sampling data of the precise magnetic field model for supervised learning, and the simulation results show the effectiveness of the proposed coil geometry learning by significantly reducing and stabilizing the computation time.

II. ALTERNATING ELECTROMAGNETIC FORCE AND TORQUE MODULATION

This section introduces the magnetic field interaction model for satellite control as preliminaries. Our mathematical notation about vector and coordination are follow: Let $\{\mathbf{a}\}$ be defined as basis vector of an arbitrary frame (A) such that $\{\mathbf{a}\} = \{\mathbf{a}_x^T, \mathbf{a}_y^T, \mathbf{a}_z^T\}^T$ and we define a_p component of an arbitrary vector $\mathbf{p} \in \mathbb{R}^3$ in this frame, i.e., $\mathbf{p} = \{\mathbf{a}\}^T a_p = \{\mathbf{b}\}^T b_p = \{\mathbf{b}\}^T C^{B/A} a_p$ where $C^{B/A} \in \mathbb{R}^{3 \times 3}$ is the coordinate transformation matrix from frame (A) to (B).

Assumption 1 (Circular Air-Core Coil). *We model the 1-axis coil as a circular air-core coil and define its dipole moment as $\mu_a \triangleq \mu_{a0} \mathbf{n}$ and $\mu_{a0} \triangleq N_t A c_a$ where the number of coil turns N_t , the area enclosed by the coil A , the current strength $c_a(t)$, and \mathbf{n} is the unit vector perpendicular to the plane of the coil.*

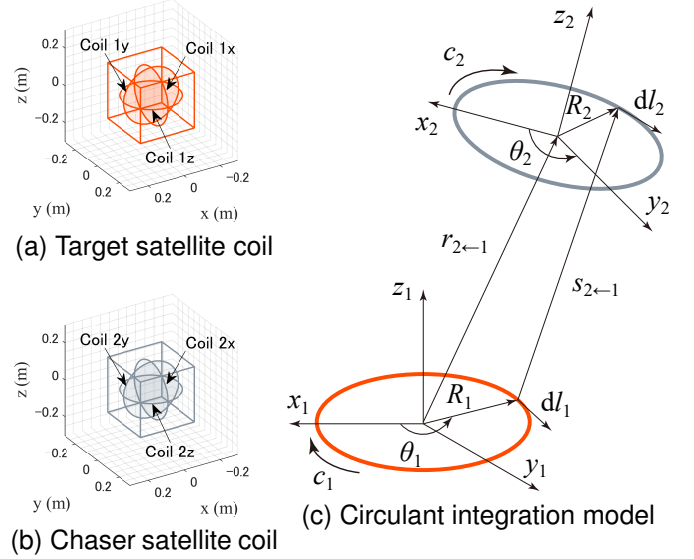


Fig. 2: The definition of 3-axis coils for target and chaser satellites. $s_{j \leftarrow k} = r_{j \leftarrow k} + C^{k/j} R_j - R_k$, $R_{i(\varphi)} = [R_i \cos \varphi, R_i \sin \varphi, 0]^T$ and $dl_{i(\varphi)} = (dR_{i(\varphi)}/d\varphi) d\varphi$.

Then, the exact magnetic field model $B(r)$ [T] [26], [31] using the well-known Biot-Savart law is

$$B(r) = \frac{\mu_0 c}{4\pi} \oint \frac{dl \times \hat{r}}{|r|^2} \in \mathbb{R}^3. \quad (1)$$

where the magnetic permeability μ_0 , the coil element $dl \in \mathbb{R}^3$, and the distance between coil elements $r \in \mathbb{R}^3$. Then, the electromagnetic force and torque experienced by the b th 1-axis coil due to the magnetic field generated by the a th 1-axis coil is

$$\begin{aligned} f_{b \leftarrow a}^{\text{coil}} &= \frac{\mu_0 \mu_{a0} \mu_{b0}}{4\pi A^2} \oint \left[\oint \frac{\mathbf{e}_{r_{ab}} \times dl_a}{\|r_{ab}\|^2} \right] \times dl_b \\ \tau_{b \leftarrow a}^{\text{coil}} &= \frac{\mu_0 \mu_{a0} \mu_{b0}}{4\pi A^2} \oint R_b \times \left[\oint \frac{\mathbf{e}_{r_{ab}} \times dl_a}{\|r_{ab}\|^2} \right] \times dl_b. \end{aligned} \quad (2)$$

where $\mathbf{e}_{r_{ab}}$ is unit vector along with r_{ab} . Figure 2 c) provides an overview of each of these parameters. We assume the satellite specification to extend the above concept:

Assumption 2 (3-axis Circular Air-Core Coil). *All n satellites have the identical circular triaxial air-core coils, such that this defines the j th dipole moment of the multi-layer coil $\mu_j(t) \in \mathbb{R}^3$ [Am^2] at time t :*

$$\mu_j(t) = \{\mathbf{b}\}^T N_t A \begin{bmatrix} c_{jx}(t) \\ c_{jy}(t) \\ c_{jz}(t) \end{bmatrix} \triangleq \{\mathbf{b}\}^T \begin{bmatrix} \mu_{jx}(t) \\ \mu_{jy}(t) \\ \mu_{jz}(t) \end{bmatrix} \quad (3)$$

where the current strength $c_{j(x,y,z)}(t)$ along with x, y, z -axis in j th body-fixed frame. Finally, we present Figure 2 illustrating the satellite model, with its center of mass coinciding with the center of the satellite.

Then, the total electromagnetic force and torque on the j -the satellites due to the neighbor satellites \mathcal{N}_j is

$$\begin{bmatrix} \mathbf{f}_j \\ \boldsymbol{\tau}_j \end{bmatrix} = \sum_{k \in \mathcal{N}_j} \begin{bmatrix} \mathbf{f}_{j \leftarrow k} \\ \boldsymbol{\tau}_{j \leftarrow k} \end{bmatrix} = \sum_{k \in \mathcal{N}_j} \sum_{\substack{a= \\ (x,y,z)}} \sum_{\substack{b= \\ (x,y,z)}} \begin{bmatrix} \mathbf{f}_{j(a) \leftarrow k(b)}^{\text{coil}} \\ \boldsymbol{\tau}_{j(a) \leftarrow k(b)}^{\text{coil}} \end{bmatrix} \quad (4)$$

III. PROBLEM FORMULATION AND DECENTRALIZED DOCKING

As shown in Figs. 2 a) and b), we refer to the 1st satellite as the target satellite and the 2nd satellite as the chaser satellite. The j -th electromagnetic force and torque due to the magnetic field generated by the k th satellite in Eq. (4): $[{}^a f_{j \leftarrow k}; {}^a \tau_{j \leftarrow k}] = \frac{\mu_0}{4\pi} {}^a Q ({}^a \mu_k \otimes {}^a \mu_j)$ where ${}^a Q \in \mathbb{R}^{6 \times 9}$

$${}^a Q = \frac{1}{A^2} \begin{bmatrix} {}^a I_{j \leftarrow k_x} & {}^a I_{j \leftarrow k_y} & {}^a I_{j \leftarrow k_z} \\ {}^a J_{j \leftarrow k_x} & {}^a J_{j \leftarrow k_y} & {}^a J_{j \leftarrow k_z} \end{bmatrix} \quad (5)$$

where ${}^a I_{j \leftarrow k_x} = [{}^a I_{j_x \leftarrow k_x}, {}^a I_{j_y \leftarrow k_x}, {}^a I_{j_z \leftarrow k_x}] \in \mathbb{R}^{3 \times 3}$ and $I_{j_x \leftarrow k_x}$ includes the circulant integration term in Eq. (2) and summarized for $w = (x, y, z)$:

$$\begin{cases} \mathbf{I}_{j_w \leftarrow k_w} = \int_{\theta_j=0}^{\theta_j=2\pi} \left[\int_{\theta_k=0}^{\theta_k=2\pi} \frac{\mathbf{e}_{r_{j \leftarrow k}} \times d\mathbf{l}_{k_w}}{\|r_{j \leftarrow k}\|^2} \right] \times d\mathbf{l}_{j_w} \\ \mathbf{J}_{j_w \leftarrow k_w} = \int_{\theta_j=0}^{\theta_j=2\pi} R_{j_w} \times \left[\int_{\theta_k=0}^{\theta_k=2\pi} \frac{\mathbf{e}_{r_{j \leftarrow k}} \times d\mathbf{l}_{k_w}}{\|r_{j \leftarrow k}\|^2} \right] \times d\mathbf{l}_{j_w}. \end{cases} \quad (6)$$

This model incorporates a circulant integration term that accounts for the relative position, relative attitude, and coil geometry; however, it has a notable drawback: a significant computational load. We finally focus on alternating current (AC) modulation in the context of multi-satellite control using magnetic fields.

Assumption 3 (Alternating current and first-order averaged dynamics). *The j th satellites use AC $c_j(t)$ for coils:*

$$\begin{aligned} c_j(t) &= c_j^{(\sin)} \sin \omega_f t + c_j^{(\cos)} \cos \omega_f t \\ \mu_j(t) &= s_j \sin \omega_f t + c_j \cos \omega_f t. \end{aligned}$$

where the AC frequency ω_f [rad/s] is the angular frequency and ω_f is sufficiently higher than the system dynamics time constant such that the first order averaging is holded, i.e., $\frac{d\bar{x}}{dt} = \int_0^T \frac{dx}{d\tau}(t, \tau) \frac{d\tau}{T} + \epsilon$ and $\epsilon \ll 1$.

Since the AC interactions fluctuate periodically, the control command values are calculated so that the average value of the electromagnetic force and torque shown in the equation matches the control value [21], [23], [25]. Then, we obtain the average values of electromagnetic force and torque between two satellites equipped with 3-axis coils:

$$\begin{aligned} \begin{bmatrix} {}^a f_{j \leftarrow k}^{(\text{avg})} \\ {}^a \tau_{j \leftarrow k}^{(\text{avg})} \end{bmatrix} &= \int_T \frac{\mu_0}{4\pi} {}^a Q ({}^a \mu_k \otimes {}^a \mu_j) \frac{d\tau}{T} \\ &\approx \frac{1}{2} \frac{\mu_0}{4\pi} {}^a Q ({}^a s_k \otimes {}^a s_j + {}^a c_k \otimes {}^a c_j) \end{aligned}$$

Finally, we derive the chaser's control currents for simultaneous control of relative position and absolute attitude as follows [32]:

$$\begin{aligned} \begin{bmatrix} {}^a f_{j \leftarrow k}^{(\text{avg})} \\ {}^a \tau_{j \leftarrow k}^{(\text{avg})} \end{bmatrix} &= \frac{1}{2} \frac{\mu_0}{4\pi} {}^a Q ([{}^a s_k, {}^a c_k] \otimes E_3) \begin{bmatrix} {}^a s_j \\ {}^a c_j \end{bmatrix} \\ \Rightarrow \begin{bmatrix} {}^a s_j \\ {}^a c_j \end{bmatrix} &= \left(\frac{1}{2} \frac{\mu_0}{4\pi} {}^a Q ([{}^a s_k, {}^a c_k] \otimes E_3) \right)^{-1} \begin{bmatrix} {}^a f_{j \leftarrow k}^{(\text{avg})} \\ {}^a \tau_{j \leftarrow k}^{(\text{avg})} \end{bmatrix} \end{aligned} \quad (7)$$

For simulation, we make the following two assumptions:

Assumption 4. *Only the 1st (target) satellite has RWs to control its attitude, and the 2nd (chaser) satellite does not. Then, the electromagnetic torque on the chaser is only controlled, and the uncontrollable electromagnetic torque due to angular momentum conservation acts on the target, which RW attenuates based on Eq. (14).*

Assumption 5. *The current amplitudes on the 1st (target) satellite are predetermined based on arbitrary constant $c_{\text{amp}0} = 3$, the relative position, and the random coefficients to ensure regularity of matrix in Eq. (7) before the decentralized current allocation in Eq. (7), i.e.,*

$$b_1 s_1 = \begin{bmatrix} c_{\text{amp}0} \frac{\|r_{12}(t)\|}{\|r_{12}(0)\|} [0.1 \quad 0.3 \quad 0.7]^T \\ c_{\text{amp}0} \frac{\|r_{12}(t)\|}{\|r_{12}(0)\|} - b_1 s_1 \end{bmatrix} \in \mathbb{R}^3. \quad (8)$$

IV. LEARNING-BASED COIL GEOMETRY APPROXIMATION

This section designs an approximate exact magnetic field model using a multilayer perceptron (MLP) model that captures coil-specific geometric features and calculates in real-time during the control. The j -th electromagnetic force and torque due to the magnetic field generated by the k th satellite is in Eq. (4) and this includes the circulant integration term in Eq. (6). This integration term consists of the relative position, relative attitude, and coil geometry. Since an obvious drawback is a heavy computational load, we approximate these coil-specific geometry terms using a multi-layer perceptron (MLP).

We first mention the sampling input and label data for the j, k th satellites. For the k th satellite, let $C^{A/B_k}(\sigma_k)$ be defined as the coordinate transformation matrix from k th body-fixed frame into the arbitrary reference frame and this is derived by arbitrary attitude parameter σ_k . We define $\mathbf{n}_{k(x,y,z)}$ as the unit vectors along with x, y, z axes such that

$${}^a n_{k_x}, {}^a n_{k_y}, {}^a n_{k_z} \triangleq \left\{ C^{A/B_k}(\sigma_k) = [{}^a n_{k_x} \quad {}^a n_{k_y} \quad {}^a n_{k_z}] \right\}$$

Our goal is to reduce the input sample space by deriving a two coordinate transformation matrix such that 1) one coil lies within the x - y plane and 2) the other coil lies within the x - z plane, as illustrated in Figure 2c (b). Then, we first define three type coordinate frame $B_{k(x,y,z)}$ such that each $\mathbf{n}_{k(x,y,z)}$ corresponds to its z -axis and its transformation matrix $C^{A/B_{k(x,y,z)}} \in \mathbb{R}^{3 \times 3}$ is defined as

$$C^{A/B_{k(z,x,y)}} \triangleq [{}^a n_{k(x,y,z)} \quad {}^a n_{k(y,z,x)} \quad {}^a n_{k(z,x,y)}] \quad (9)$$

where $C^{A/B_k}(\sigma_k) = C^{A/B_{k_z}}$. This achieves the first goal, and the following transformation achieves the second goal:

$$C^{D_{j \leftarrow k_w}/B_{k_w}} \triangleq \begin{bmatrix} \cos \theta_0 & \sin \theta_0 & 0 \\ -\sin \theta_0 & \cos \theta_0 & 0 \\ 0 & 0 & \text{sgn}({}^{b_{k_w}} r_{j \leftarrow k(z)}) \end{bmatrix} \quad (10)$$

$$\theta_0 = \theta_{b_{k_w}} \triangleq \tan^{-1} ({}^{b_{k_w}} r_{j \leftarrow k(y)}, {}^{b_{k_w}} r_{j \leftarrow k(x)})$$

These two coordinate transformation defines $C^{D_{j \leftarrow k_w}/A} = C^{D_{j \leftarrow k_w}/B_{k_w}} C^{B_{k_w}/A}$ for $w = (x, y, z)$:

$$\begin{aligned} [{}^d r_{j \leftarrow k} \quad {}^d n_{j_w}] &= C^{D_{j \leftarrow k_w}/A} [{}^a r_{j \leftarrow k} \quad {}^a n_{j_w}] \\ [{}^d I_{j_w \leftarrow k_w} \quad {}^d J_{j_w \leftarrow k_w}] &= C^{D_{j \leftarrow k_w}/A} [{}^a I_{j_w \leftarrow k_w} \quad {}^a J_{j_w \leftarrow k_w}] \end{aligned}$$

Note that coordinate transformation $C^{D_{j \leftarrow k_w}/B_{k_w}}$ imposes ${}^{d_{k_w}}r_{j \leftarrow k(1)} = 0$ and, thus, we reduce this component for input data as ${}^{d_{k_w}}\hat{r}_{j \leftarrow k} = [{}^{d_{k_w}}r_{j \leftarrow k(1)}; {}^{d_{k_w}}r_{j \leftarrow k(3)}]$. The spherical coordinate system using azimuth $\phi_{(1)} \in [-\pi, \pi]$ and elevation $\phi_{(2)} \in [0, \pi]$ reduces the 3-dimensional information into $\phi \in \mathbb{R}^2$ such that

$$\phi \triangleq \left[\begin{array}{c} \tan^{-1}({}^{d_{k_w}}n_{j_w(2)}, {}^{d_{k_w}}n_{j_w(1)}) \\ \cos^{-1}({}^{d_{k_w}}n_{j_w(3)}) \end{array} \right] = \left\{ \phi \mid {}^{d_{k_w}}n_{j_w} \triangleq \left[\begin{array}{c} c_{\phi_{(1)}} s_{\phi_{(2)}} \\ s_{\phi_{(1)}} s_{\phi_{(2)}} \\ c_{\phi_{(2)}} \end{array} \right] \right\}$$

As a result, our sampling datas $X = [\mathbf{r}, \phi] \in \mathbb{R}^{N_s \times 4}$ and $Y \in \mathbb{R}^{N_s \times 6}$ are stuck as follows:

$$\mathbf{r} = \left[\begin{array}{c} d_{\hat{r}_{j \leftarrow k}^{(1)}}^\top \\ \vdots \\ d_{\hat{r}_{j \leftarrow k}^{(N_s)}}^\top \end{array} \right], \phi = \left[\begin{array}{c} \phi^{(1)\top} \\ \vdots \\ \phi^{(N_s)\top} \end{array} \right], \mathbf{Y} = \left[\begin{array}{c} [dI_{j_z \leftarrow k_z}^{(1)\top}, dJ_{j_z \leftarrow k_z}^{(1)\top}] \\ \vdots \\ [dI_{j_z \leftarrow k_z}^{(N_s)\top}, dJ_{j_z \leftarrow k_z}^{(N_s)\top}] \end{array} \right]$$

where N_s is the number of samples. Our MLP represents the functional mapping from given inputs x into some outputs $\mathcal{Y}_{(\mathbf{X}, \theta)}^{(j)}$ such as a $(L+1)$ -layer neural network and we train to minimize arbitrary loss function $f(\cdot)$:

$$\theta_w^*, \theta_b^* = \operatorname{argmin} \sum_{j=1}^{N_s} f \left(\left\| \mathbf{Y}^{(j)\top} - \mathcal{C}^\top(X^{(j)}, \theta) \right\| \right)$$

$$\mathcal{C}(\mathbf{X}^{(j)}, \theta) = W^{L+1} \phi(\dots \phi(W^1 X^{(j)} + b^1) \dots) + b^{L+1} \quad (11)$$

where the activation function $\phi(\cdot)$ and the MLP parameters θ include the MLP weights $\theta_w = W^1, \dots, W^{L+1}$ and the MLP bias $\theta_b = b^1, \dots, b^{L+1}$, and $\mathcal{C}(\mathbf{X}^{(j)}, \theta)$ is a estimated value.

We can generalize these coil geometry learning results, i.e., . The pseudocode for offline training and online inference is presented in Algorithm 1.

Corollary 1. Let $\mathcal{C}(\mathbf{X}, \theta)$ be a function mapping in Eq. (11) for given coil radius $R_{[1]}$ using a training data set $\mathcal{T}_{R_{[1]}} = \{(X_{[1]}^{(i)} = [r_{[1]}^{(i)}, \phi^{(i)}], Y_{[1]}^{(i)}(X_{[1]}^{(i)}))\}_{i=1}^N$ sampled in sample region of given compact set $\mathcal{S}_{R_{[1]}}$:

$$\mathcal{S}_{R_{[1]}} = \left\{ \begin{array}{l} r_{[1]} \in \mathbb{R}^2 \\ \phi \in \mathbb{R}^2 \end{array} \mid 2R_{[1]} < r \leq \|r_{[1]}\| \leq \bar{r}, \begin{array}{l} \phi_{(1)} \in [-\pi, \pi] \\ \phi_{(2)} \in [0, \pi] \end{array} \right\}.$$

Consider the coil whose radius is $R_{[2]}$ and and the new data

$$R_{[2]} \triangleq \gamma R_{[1]}, \left\{ X_{[2]}^{(i)} = [r_{[2]}^{(i)}, \phi^{(i)}], Y_{[2]}^{(i)}(X_{[2]}^{(i)}) \right\}_{i=1}^N$$

in sample region of given compact set $\mathcal{S}_{R_{[2]}}$ that bounded by constants of $\mathcal{S}_{R_{[1]}}$:

$$\mathcal{S}_{R_{[2]}} = \left\{ \begin{array}{l} r_{[2]} \in \mathbb{R}^2 \\ \phi \in \mathbb{R}^2 \end{array} \mid 2R_{[1]} < r \leq \frac{\|r_{[2]}\|}{\gamma} \leq \bar{r}, \begin{array}{l} \phi_{(1)} \in [-\pi, \pi] \\ \phi_{(2)} \in [0, \pi] \end{array} \right\}.$$

Then, $\mathcal{C}(\mathbf{X}^{[1]}, \theta)$ for $R_{[1]}$ coil can be applied to obtain the coil geometry information of $R_{[2]}$ in Eq. (6) as

$$Y_{[2]}^{(i)}(X_{[2]}^{(i)}) = \left[\begin{array}{c} \mathbf{I}_{[2]j \leftarrow k} \\ \mathbf{J}_{[2]j \leftarrow k} \end{array} \right] = \mathcal{C}(\mathbf{r}_{[2]}^{(i)}/\gamma, \phi_{[2]}^{(i)}, \theta) \left[\begin{array}{cc} I & O \\ O & \gamma I \end{array} \right] \quad (12)$$

where $\mathcal{C}(\mathbf{X}, \theta) = \mathcal{C}([\mathbf{r}, \phi], \theta)$.

Algorithm 1 Coil geometry learning

- 1: — **Offline Phase** —
 - 2: **Inputs:** 1) index $i \in [1, n_s]$, 2) relative position ${}^a r_{j \leftarrow k}^{(i)}$ in reference frame (A), 3) unit vectors ${}^a n_{j, k(x, y, z)}^{(i)}$ of the j, k th body-fixed frame
 - 3: **Outputs:** MLP weights θ_w^* , MLP bias θ_b^*
 - 4: **for** $i \in [1, \dots, n_s]$ **do**
 - 5: Derive $C^{A/B_{k_z}} = [{}^a n_{k_x}, {}^a n_{k_y}, {}^a n_{k_z}]$ in Eq. (9)
 - 6: Derive $C^{D_{j \leftarrow k_z}/B_{k_z}}(C^{B_{k_z}/A} {}^a r_{j \leftarrow k}^{(i)})$ in Eq. (10)
 - 7: Stack inputs $\mathbf{x}^{(f)} = [{}^{d_{j \leftarrow k_z}}r_{j \leftarrow k}^{(i)}; {}^{d_{j \leftarrow k_z}}n_{j_z}^{(i)}]^\top$
 - 8: Calculate ${}^a I_{j_z \leftarrow k_z}$ and ${}^a J_{j_z \leftarrow k_z}$ in Eq. (6)
 - 9: Stack labels $\mathbf{y}^{(f)} = [{}^{d_{j \leftarrow k_z}}I_{j_z \leftarrow k_z}; {}^{d_{j \leftarrow k_z}}J_{j_z \leftarrow k_z}]^\top$
 - 10: **end for**
 - 11: Excute Eq. (11) to derive θ_w^*, θ_b^* by \mathbf{x} and \mathbf{y}
 - 12: — **Online Phase** —
 - 13: **Inputs:** 1) ${}^a r_{j \leftarrow k}$, 2) ${}^a n_{j, k(x, y, z)}$, 3) θ_w^*, θ_b^*
 - 14: **Outputs:** Near-filed coefficient matrix ${}^a Q_{j \leftarrow k} \in \mathbb{R}^{6 \times 9}$
 - 15: **for** $l \in [x, y, z]$ **do**
 - 16: Derive $C^{A/B_{k_l}}({}^a n_{k(x, y, z)})$ in Eq. (9)
 - 17: Derive $C^{D_{j \leftarrow k_l}/B_{k_l}}(C^{B_{k_l}/A} {}^a r_{j \leftarrow k})$ in Eq. (10)
 - 18: **for** $m \in [x, y, z]$ **do**
 - 19: Calculate $[{}^{d_{j \leftarrow k_l}}I_{j_m \leftarrow k_l}; {}^{d_{j_m \leftarrow k_l}}J_{j_m \leftarrow k_l}]^\top = f(x, \theta)$ in Eq. (6) where $x = [{}^{d_{j \leftarrow k_l}}r_{j \leftarrow k}; {}^{d_{j \leftarrow k_l}}n_{j_m}]^\top$
 - 20: Calculate $[{}^a I_{j_m \leftarrow k_l}; {}^a J_{j_m \leftarrow k_l}]^\top$
 - 21: **end for**
 - 22: Stack ${}^a K_{j \leftarrow k_l} = [{}^a K_{j_x \leftarrow k_l}, {}^a K_{j_y \leftarrow k_l}, {}^a K_{j_z \leftarrow k_l}] \in \mathbb{R}^{3 \times 3}$ for $K = \{I, J\}$
 - 23: **end for**
 - 24: Stack ${}^a Q_{j \leftarrow k} = \left[\begin{array}{ccc} {}^a I_{j \leftarrow k_x} & {}^a I_{j \leftarrow k_y} & {}^a I_{j \leftarrow k_z} \\ {}^a J_{j \leftarrow k_x} & {}^a J_{j \leftarrow k_y} & {}^a J_{j \leftarrow k_z} \end{array} \right] \in \mathbb{R}^{6 \times 9}$
-

Proof. For given $R_{[1]}$ and $R_{[2]}$, recall and redefine $r_{[k]ij}$, $R_{[k]i(\varphi)}$, and $dl_{[k]i(\varphi)} = (dR_{[k]i(\varphi)}/d\varphi)d\varphi$ in Eq. (2) for $k = 1, 2$. Then, we concludes Eq. (12) by

$$\mathbf{I}_{[2]j \leftarrow k} = \int_{\theta=0}^{\theta=2\pi} \left[\int_{\varphi=0}^{\varphi=2\pi} \frac{e_{r_{j \leftarrow k}} \times dl_{[1]k}}{\|r_{[2]j \leftarrow k}/\gamma\|^2} \right] \times dl_{[1]j}$$

$$\mathbf{J}_{[2]j \leftarrow k} = \int_{\theta=0}^{\theta=2\pi} \frac{R_{[1]j}}{\gamma} \times \left[\int_{\varphi=0}^{\varphi=2\pi} \frac{e_{r_{j \leftarrow k}} \times dl_{[1]k}}{\|r_{[2]j \leftarrow k}/\gamma\|^2} \right] \times dl_{[1]j}$$

where $r_{[2]j \leftarrow k}/\gamma$ is associated with $r_{[1]j \leftarrow k}$ and we omit the index w for simplicity. \square

A. Offline Training of Generalized Coil Geometry Learning

We collect approximately 10 million samples and train our MLP using supervised learning. $R_{[2]} = 0.15.r = 0.74$, $R_{[3]} = 0.30.r = 2.1$. To explore network compactness, we train the model with two hidden layers, each with 256 and 128 neurons, respectively. Each layer follows Layer Normalization and GELU activation. The output layer maps directly to the target dimension. The loss function $f(\cdot)$ in Eq. (11) is the Smooth L1 loss. We used the Adam optimizer with an initial learning rate of $3e^{-3}$ and applied cosine annealing learning rate scheduling to improve convergence. The parameters were set as follows: $T_{\max} = 300$ and a minimum learning rate of

$1e^{-12}$. The model was trained for 300 epochs with a batch size of 8192. The training process resulted in convergence with a test loss of $4.11e^{-3}$ and a training loss of $3.01e^{-3}$. This close agreement implies acceptable generalization performance. On the validation PC, the average value of the cyclic integral in Eq. (6) decreased from 121.2 ms to 29.5 ms over one million iterations. Furthermore, the standard deviation of the computation time was reduced from 176 ms to 11.3 ms, indicating more stable and consistent computation. To quantitatively evaluate the prediction accuracy of the proposed model, we employ four standard regression metrics: the coefficient of determination (R^2), mean absolute error (MAE), root mean squared error (RMSE), and maximum absolute error (MaxE). These metrics are defined as follows:

$$R^2 = 1 - \frac{\sum_{i=1}^N (y_i - \hat{y}_i)^2}{\sum_{i=1}^N (y_i - \bar{y})^2}, \quad \text{MAE} = \frac{1}{N} \sum_{i=1}^N |y_i - \hat{y}_i|$$

$$\text{RMSE} = \sqrt{\frac{1}{N} \sum_{i=1}^N (y_i - \hat{y}_i)^2}, \quad \text{MaxE} = \max_{i=1, \dots, N} |y_i - \hat{y}_i|$$

where $y^{(i)}$ and $\hat{y}^{(i)}$ denote the ground truth and predicted values, respectively, for the i -th sample, \bar{y} is the mean of the ground truth values, and N is the total number of samples. The R^2 score represents how well the model explains the variance in the data, with $R^2 = 1$ indicating perfect prediction. MAE and RMSE evaluate the average prediction error, where RMSE penalizes larger errors more strongly. MaxE captures the most significant single deviation between prediction and ground truth. In our experiments, all models achieved R^2 scores greater than 0.97, with MAE and RMSE values typically below 0.16. MaxE remained within acceptable bounds in most cases, highlighting the model's robustness even in the presence of occasional outliers.

V. NUMERICAL AND EXPERIMENTAL VALIDATION

This section validates the proposed learning-based current calculation by applying it to the satellite's relative position and absolute attitude control, i.e., docking control.

A. Numerical Validation for Satellite Docking Scenario

This subsection validates the coil geometry learning by two satellite docking simulations. The position and attitude controllers are PD controllers designed using a coefficient diagram method [33] and executed at 0.1-second intervals. At each time, we update the target values for the controller based on the final target values using third-order splines to suppress control current fluctuations. Thanks to the generated target value profile, we have successfully constrained the current within acceptable limits in simulation, avoiding exceeding the set upper limit of $\pm 10A$. Table I summarizes the satellite specifications and orbit altitudes. Note that we observed the conservation of angular momentum for all simulations, affirming the validity of our simulation. The initial values and final target values are summarized in Table II. As stated in the assumptions, the target satellite applies the predetermined current in Eq. (8), and the chaser satellite calculates its current

TABLE I: The satellite specifications and earth orbit altitudes.

Parameters	Values	Parameters	Values
Coil radius	0.15 m	Coil turns	100
Satellite mass	20 kg	Altitude	700 km
AC amplitude limit	± 10 A	AC frequency	8π rad/s

TABLE II: Initial and final target values.

Parameters	Values
Relative position	$[0.3, -0.4, 0.6]^T$ m
Relative velocity	$[0, 0, 0]^T$ m
Angular velocity (S/C 1)	$[0.01, 0.02, 0.08]^T$ rad/s
Angular velocity (S/C 2)	$[1e^{-4}, 2e^{-4}, 8e^{-4}]^T$ rad/s
Quaternion	$[0, 0, 0, 1]^T$
Target Relative position	$[0, 0, 0.3]^T$ m
Target Angular velocity	$[0, 0, 0]^T$ m
Target Quaternion	$[0, 0, 0, 1]^T$

in the decentralized manner in Eq. (7). We note that the actual magnetic field calculation is conducted by the near-field model for all numerical calculations.

We first compare the docking results based on the far-field approximation model in Eq. (15) and the exact model in Eq. (1) to highlight the effectiveness of the near-field model. Figure 3 presents an overview of the three-dimensional simulation results, and the target satellite values are depicted in gray, and the chaser satellite in red. Figure 3 (a,b) are the control results using the far-field model-based calculation (see the details of the calculation based on the far-field approximation in Appendix B). Figure 4 shows the time evolution of the position and attitude states and electromagnetic control inputs. Dashed lines represent results based on the far-field model, while solid lines represent those based on the near-field model. We can observe that significant control input errors occur between the two models at approximately 250 seconds. This extensive control effort leads to a collision as shown in Fig. 3 (b). Conversely, Fig. 3 (c) shows that employing the near-field Model enables both relative distance and absolute attitude control through magnetic field interaction, even at proximity for randomly generated 40 initial states. Here, the 1st satellite accomplishes attitude control using reaction wheels, based on Eq. (14), to converge its attitude to the target and mitigate electromagnetic torque disturbances. It is worth noting 2nd satellite achieves attitude control only by using electromagnetic torque without reaction wheels that reaffirms the effectiveness of employing electromagnetic torque for attitude control [23]–[25], [32], [34].

VI. CONCLUSIONS

This paper proposes a learning-based magnetic field model that imitates the exact model of magnetic fields and applies it to pollution-free docking, considering the fuel limitations and proximity disturbance avoidance. We first develop a decentralized current calculation that considers the coil offset without inter-satellite communications. We propose a learning-based magnetic field approximation to overcome the high computational burden of the exact model and the model error of the far-field approximation in close proximity. In the simulation, we demonstrate that the traditional approximation,

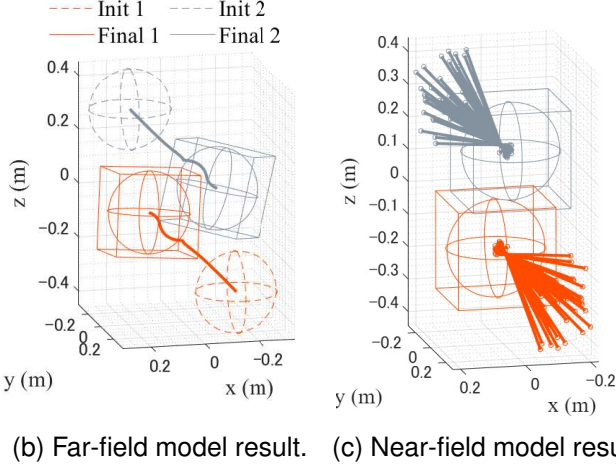
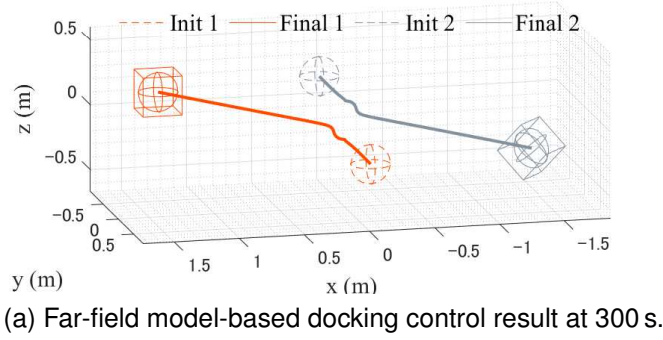


Fig. 3: The docking control results of two satellites using the far-field approximation in Eq. (15) and exact model in Eq. (1): a) overview of the far-field model control during 300 s, b) positions of far-field model control result at 250 s, and c) near-field model results for 40 random initial conditions.

the far-field model, fails to achieve target values in close proximity, leading to collisions. In contrast, our learning-based magnetic field model achieves simultaneous control of relative distance and attitude with small computational load and stability. Applications of this magnetic docking include the propulsion-assisted or fuel-free docking for resource-limited small satellites, such as assembling large structures and space solar power generators. This can lower launch frequency and save costs.

APPENDIX

A. Orbital and Attitude Motion of an Earth Orbiting Satellite

This subsection introduces the relative motion and attitude dynamics using RW. The relative motion of two satellites orbiting in a circular orbit is denoted in the orbital coordinate system $\{o\}$ frame:

$$\begin{aligned} \ddot{x} + 2\omega_o \dot{y} - 3\omega_o^2 x &= \frac{F_x}{m_c} \\ \ddot{y} - 2\omega_o \dot{x} &= \frac{F_y}{m_c}, \quad \ddot{z} + \omega_o^2 z = \frac{F_z}{m_c} \end{aligned} \quad (13)$$

where $m_c \in \mathbb{R}$ represents the mass of the chaser satellite, $\omega_o \in \mathbb{R}$ denotes the orbital frequency given by $\omega_o = \sqrt{\mu_g/R_o^3} \in \mathbb{R}$ with the geocentric gravitational constant $\mu_g \in \mathbb{R}$ and the

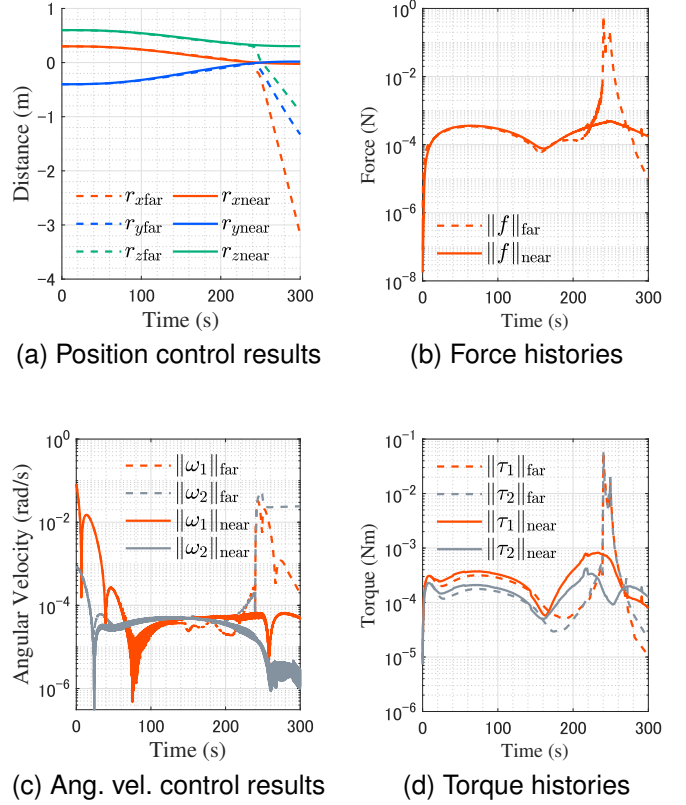


Fig. 4: Two-satellite docking control using the far-field magnetic field approximation in Eqs. (15) and the exact magnetic field model in Eqs. (1): a), c) Position and attitude control results; b), d) Electromagnetic force and torque histories.

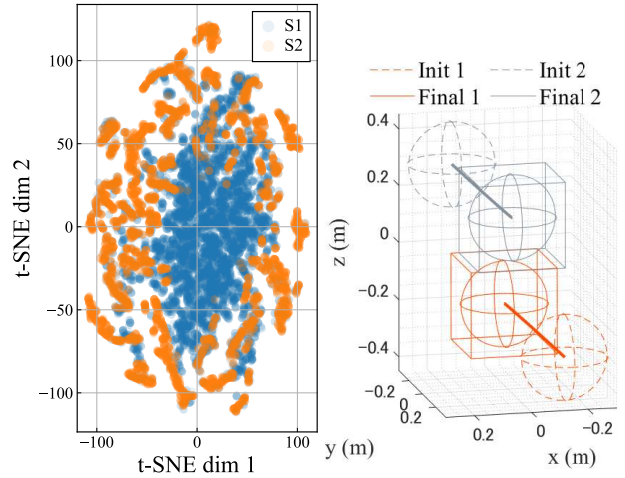


Fig. 5: Docking control results using the exact near-field model in Eqs. (1) and (2): a) sample docking control region for training and docking : $0.2 \leq \|r\| \leq 1$, b) trajectories under the learning-based controller for 40 random initial conditions.

satellite's orbital radius $R_o \in \mathbb{R}$. Note that this study mainly focuses on the actuator level problem, and then, the inter-satellite distance is set to a relatively small value to neglect the dynamics effect. Finally, the following equation shows the

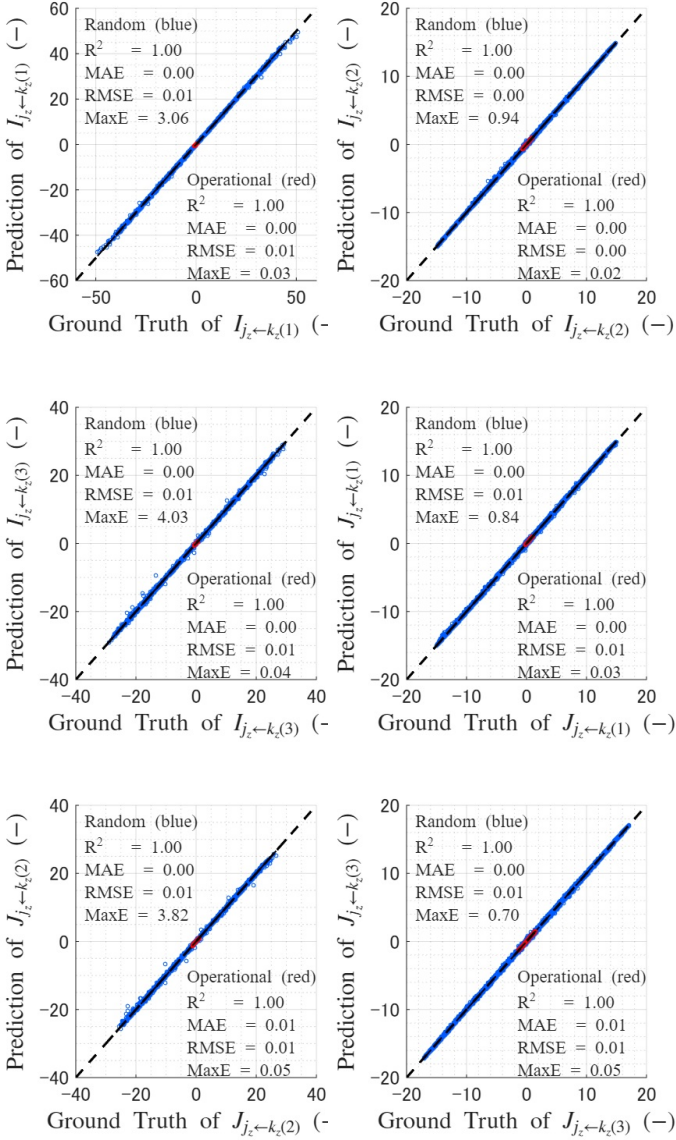


Fig. 6: The ground-truth label data obtained from direct computation and the values predicted by the MLP. The predictions of the circulant integration term in Eq. (6) for randomly generated docking trajectories.

attitude dynamics for a satellite equipped with a reaction wheel (RW):

$$J \cdot \dot{\omega} + \omega \times (J \cdot \omega + h_{RW}) = -\tau_{RW} + \tau_d, \quad \dot{h}_{RW} = \tau_{RW} \quad (14)$$

where $J \in \mathbb{R}^{3 \times 3}$ is the moment of inertia, $\omega \in \mathbb{R}^3$ is the aircraft angular velocity, $h_{RW} \in \mathbb{R}^3$ and τ_{RW} are the angular momentum of RW and torque, and $\tau_d \in \mathbb{R}^3$ is the disturbance torque.

B. “Far-field” Approximation Model

“Far-field” model [26] provides a computationally friendly approximated magnetic field. We define the relative vector $s_{ij} \in \mathbb{R}^3$ between the geometric center of two coils, and the position vector $R_i \in \mathbb{R}$ from the geometric center into dl_i

such that $r_{ij} = s_{ij} - R_i$. We assume the size of the coil loop is much smaller than the relative distance, i.e., $|R_i| \ll |s_{ij}|$. Then, we get

$$|R_i| \ll |s_{ij}| \Rightarrow \frac{1}{|r|} \approx \frac{1}{|s_{ij}|} + \frac{s_{ij} \cdot R_i}{|s_{ij}|^3}$$

This approximation convert the multi-layer coil derives dipole model, i.e., j th magnetic moment $\mu_j(t) \in \mathbb{R}^3$ [Am²] at time t and its magnetic field $B_k(\mu_k, r_{jk}) \in \mathbb{R}^3$ [T] are

$$B_k(\mu_k, r_{jk}) = \frac{\mu_0}{4\pi d_{jk}^3} (3M_k e_r - \mu_k) \quad (15)$$

where μ_k is in Eq. (3), $M_k = \mu_k \cdot e_r$, $d_{jk} = \|r_{jk}\|$, and $e_r = r_{jk}/d_{jk}$. This model is accurate if the relative distance s_{ij} exceeds around twice the diameter of the coil, i.e., $2R_i$ [30]. This also simplifies the magnetic field interaction model, the electromagnetic force and torque exerted on the j -th agent by the k -th one as $f_{j \leftarrow k}(\mu_{j,k}, r_{jk}) = \nabla(\mu_j \cdot B_k)$ and $\tau_{j \leftarrow k}(\mu_{j,k}, r_{jk}) = \mu_j \times B_k$ where

$$f_{j \leftarrow k} = \frac{3\mu_0}{4\pi d^4} ((\mu_k \cdot \mu_j - 5M_k M_j) e_r + M_k \mu_j + M_j \mu_k). \quad (16)$$

REFERENCES

- [1] R. C. Foust, E. S. Lupu, Y. K. Nakka, S.-J. Chung, and F. Y. Hadaegh, “Ultra-soft electromagnetic docking with applications to in-orbit assembly,” in *69th International Astronautical Congress, Bremen, Germany*, 2018, pp. 1–5.
- [2] W. K. Belvin, W. R. Doggett, J. J. Watson, J. T. Dorsey, J. E. Warren, T. C. Jones, E. E. Komendera, T. Mann, and L. M. Bowman, “In-space structural assembly: Applications and technology,” in *3rd AIAA Spacecraft Structures Conference*, 2016, p. 2163.
- [3] J. Dorsey and J. Watson, “Space assembly of large structural system architectures (salssa),” in *AIAA SPACE 2016*, 2016, p. 5481.
- [4] T. Inamori, P. Ji-Hyun, K. Nagai, H. Tamura, G. Xinbo, Y. Fujita, R. Yamaguchi, T. Miyamoto, D. Ukita, T. Osaki *et al.*, “In-orbit demonstration of propellant-less formation flight with momentum exchange of jointed multiple cubesats in the magnaro mission,” 2022.
- [5] C. Blackerby, A. Okamoto, S. Iizuka, Y. Kobayashi, K. Fujimoto, Y. Seto, S. Fujita, T. Iwai, N. Okada, J. Forshaw *et al.*, “The elsa-d end-of-life debris removal mission: Preparing for launch,” in *Proceedings of the International Astronautical Congress, IAC*, vol. 8, 2019.
- [6] T. Shibata, T. Bennett, and H. Schaub, “Prospects of a hybrid magnetic/electrostatic sample container retriever,” *Journal of Spacecraft and Rockets*, vol. 57, no. 3, pp. 434–445, 2020.
- [7] Z. Manchester, M. Peck, and A. Filo, “Kicksat: A crowd-funded mission to demonstrate the world’s smallest spacecraft,” in *In Proceedings of the 27th AIAA/USU Conference, Small Satellite Constellations*, 2013.
- [8] F. Y. Hadaegh, S.-J. Chung, and H. M. Manohara, “On development of 100-gram-class spacecraft for swarm applications,” *IEEE Systems Journal*, vol. 10, no. 2, pp. 673–684, 2014.
- [9] D. Tuzi, T. Delamotte, and A. Knopp, “Satellite swarm-based antenna arrays for 6g direct-to-cell connectivity,” *IEEE Access*, vol. 11, pp. 36 907–36 928, 2023.
- [10] S. Morioka, T. Inagawa, N. Homma, K. Murata, H. Yamaguchi, A. Shirane, M. Okada, K. Yasumoto, and M. Kim, “Dense formation flying of multiple picosats for communication satellites and its technical challenges,” *IEICE Technical Report; IEICE Tech. Rep.*, vol. 124, no. 289, pp. 49–54, 2024.
- [11] Y. Takahashi, S. Shim, and S.-i. Sakai, “Distance-based relative orbital transition for palm-sized satellite swarm with guaranteed escape-avoidance,” in *AIAA Scitech 2025 Forum*, 2025, p. 2068.
- [12] S. Shim, Y. Takahashi, N. Usami, M. Kubota, and S.-i. Sakai, “Feasibility analysis of distributed space antennas using electromagnetic formation flight,” in *2025 IEEE Aerospace Conference*, 2025.
- [13] R. C. Foust, “Optimal guidance and control of heterogeneous swarms for in-orbit self-assembly of large space structures: Algorithms and experiments,” Ph.D. dissertation, University of Illinois at Urbana-Champaign, 2019.

- [14] G. Cai, L. Liu, B. He, G. Ling, H. Weng, and W. Wang, "A review of research on the vacuum plume," *Aerospace*, vol. 9, no. 11, p. 706, 2022.
- [15] G. Dettleff and M. Grabe, "Basics of plume impingement analysis for small chemical and cold gas thrusters," *Models and Computational Methods for Rarefied Flows*, 2011.
- [16] M. Grabe and C. E. Soares, "Status and future of research on plume induced contamination," in *Proceedings of the International Astronautical Congress, IAC*. IAF, 2019.
- [17] B. He, J. Zhang, and G. Cai, "Research on vacuum plume and its effects," *Chinese Journal of Aeronautics*, vol. 26, no. 1, pp. 27–36, 2013.
- [18] W. Fehse, *Automated Rendezvous and Docking of Spacecraft*. Cambridge University Press, 2003, vol. 16.
- [19] S.-I. Sakai, Y. Fukushima, and H. Saito, "Design and on-orbit evaluation of magnetic attitude control system for the "reimei" microsatellite," in *10th IEEE International Workshop on Advanced Motion Control*. IEEE, 2008, pp. 584–589.
- [20] T. Shibata and S.-I. Sakai, "A contactless micro-vibration isolator using the flux pinning effect for space telescopes," *Journal of Spacecraft and Rockets*, vol. 59, no. 2, pp. 651–659, 2022.
- [21] Y. Takahashi, H. Sakamoto, and S.-i. Sakai, "Kinematics control of electromagnetic formation flight using angular-momentum conservation constraint," *Journal of Guidance, Control, and Dynamics*, vol. 45, no. 2, pp. 280–295, 2022.
- [22] R. Kaneda, S.-I. Sakai, T. Hashimoto, and H. Saito, "The relative position control in formation flying satellites using super-conducting magnets," *Japan Society of Aeronautical Space Sciences*, vol. 56, no. 652, pp. 203–210, 2008.
- [23] Y. Takahashi, H. Sakamoto, and S.-i. Sakai, "Simultaneous control of relative position and absolute attitude for electromagnetic spacecraft swarm," in *AIAA Scitech 2021 Forum*, 2021, p. 1104.
- [24] A. Ayyad, "Optimal guidance and control for electromagnetic formation flying," Master's thesis, The University of Tokyo, 2019.
- [25] Y. Takahashi, H. Sakamoto, and S.-i. Sakai, "Control law of electromagnetic formation flight utilizing conservation of angular momentum: Time-varying control without using additional attitude actuator," in *The 30th Workshop on JAXA Astrodynamics and Flight Mechanics*. Japan Aerospace Exploration Agency / Institute of Space and Astronautical Science, 2020. [Online]. Available: <https://jaxa.repo.nii.ac.jp/records/47545>
- [26] S. A. Schweighart, "Electromagnetic formation flight dipole solution planning," Ph.D. dissertation, Massachusetts Institute of Technology, 2005.
- [27] S.-i. Sakai, R. Kaneda, K. Maeda, T. Saitoh, H. Saito, and T. Hashimoto, "Electromagnetic formation flight for leo satellites," in *3rd International Symposium on Formation Flying, Missions and Technologies*, 2008.
- [28] U. Ahsun, "Dynamics and control of electromagnetic satellite formations," Ph.D. dissertation, Massachusetts Institute of Technology, Aeronautics and Astronautics Department, 2007.
- [29] A. K. Porter, D. J. Alinger, R. J. Sedwick, J. Merk, R. A. Opperman, A. Buck, G. Eslinger, P. Fisher, D. W. Miller, and E. Bou, "Demonstration of electromagnetic formation flight and wireless power transfer," *Journal of Spacecraft and Rockets*, vol. 51, no. 6, pp. 1914–1923, 2014.
- [30] A. Sakaguchi, "Micro-electromagnetic formation flight of satellite systems," Ph.D. dissertation, Massachusetts Institute of Technology, 2005.
- [31] H. Tajima, Y. Takahashi, T. Shibata, H. Sakamoto, and S.-i. Sakai, "Study on short range formation flight and docking control using ac magnetic field," in *74th International Astronautical Congress, Baku, Azerbaijan*, 2-6 October 2023.
- [32] Y. Takahashi, "Neural power-optimal magnetorquer solution for multi-agent formation and attitude control," 2024.
- [33] S. Manabe, "Coefficient diagram method," *IFAC Proceedings Volumes*, vol. 31, no. 21, pp. 211–222, 1998.
- [34] Z. Abbasi, J. B. Hoagg, and T. M. Seigler, "Decentralized electromagnetic formation flight using alternating magnetic field forces," *IEEE Transactions on Control Systems Technology*, vol. 30, no. 6, pp. 2480–2489, 2022.